Chapter 2
Polymer Microbead-Templated Nanostructures

Cheng Fang and Youhong Tang

Abstract In this chapter, nanostructures templated by polymer microbead, which is usually made of polystyrene with a diameter range of 300 nm–1 μm, are reviewed. We first focus on formation of the microbead monolayer in terms of the driving force for self-assembly, the junction among the neighbouring microbeads and the uniformity of microbead monolayer. Then, we discuss applications of microbead monolayer as a template for nanostructure fabrication. Because the assembled monolayer features an ordered structure scaling up to centimetre (cm) size, microbead-templated nanostructures also show an ordered arrangement in cm size, which is attractively simple and can be achieved in common laboratories. From the microbead monolayer template, the subsequent fabrication approaches include electrochemical deposition, sputter coating deposition, plasma etching, annealing, wet etching and dry etching as well. The templating targets include metals, semiconductors, polymers, and nano-moieties such as nanobeads and nanocubes. Various types of nanostructure have been fabricated using these approaches individually or by combining them to increase the flexibility of fabrication. Controllable and ordered nanostructures have been achieved by adjusting the fabrication parameters. Finally, we review the application of nanostructures templated by the polymer microbeads, particularly as surface-enhanced Raman scattering (SERS) substrates. We demonstrate approaches for identifying the position of the hot spot and how to achieve single-molecule detection.

C. Fang (✉)
Global Centre for Environmental Remediation (GCER),
University of Newcastle, Newcastle, NSW 2308, Australia
e-mail: cheng.fang@newcastle.edu.au

Y. Tang
School of Computer Science Engineering and Mathematics, Centre for Nanoscale Science and Technology, Flinders University, Adelaide, SA 5042, Australia
e-mail: youhong.tang@flinders.edu.au

Z. Lin et al. (eds.), *Polymer-Engineered Nanostructures for Advanced Energy Applications*, Engineering Materials and Processes,
DOI 10.1007/978-3-319-57003-7_2

2.1 Introduction

Polymer microbeads have been studied for decades, focusing on self-assembly into monolayers and then used as templates for the fabrication of nanostructures [1, 2]. The technique of nanosphere lithography (NSL) is economic and simple, which enables general laboratories to fabricate nanostructures without clean room support. The self-assembly of polymer microbeads means that an ordered structure can be generated. Consequently, the fabricated nanostructures are ordered, not random. Furthermore, from the ordered templates, many versatile nanostructures can be fabricated by fine-tuning the subsequent fabrication approach, using means such as deposition, etching and annealing. Basically, imagination need not be restricted, and newly fabricated nanostructures are frequently reported.

Fabricated nanostructures have demonstrated surprising properties that cannot be expected from macro-structures or bulk. Besides their large surface area, nanostructures display nanosize-related enhancements resulting in catalytic activity, as well as quantum and plasmonic resonance effects. Here, we also discuss the applications as surface-enhanced Raman scattering (SERS) substrates.

2.2 Microbead Monolayer

2.2.1 Polymer Microbeads and Silica Microbeads

Polymer microbeads are usually made of polystyrene (PS), which differ from silica microbeads. Silica is an inorganic material and is therefore more stable than PS, chemically and thermally. When used as a sensor, such as a SERS substrate, the silica itself might feature a background cleaner than that of PS, except for the two main peaks positioned around 519 and 900–1100 cm^{-1} [3]. However, the stable property of silica microbeads might restrict their flexibility for the fabrication of nanostructures. For example, when thermal annealing is selected to follow the microbead templating, a PS microbead template could be easily burnt off and removed due to organic components, whereas this did not occur with silica [4]. However, we recognise the similarity between polymer and silica microbeads in terms of microsphere lithography templating nanostructures. In this chapter, we focus our discussion on polymer microbeads.

2.2.2 Microbead Monolayer and Multilayers

Generally, a monolayer of microbeads is used as a template for the fabrication of a nanostructure, although a multilayer might also be useful [5, 6]. However, the forming conditions of microbead multilayers are difficult to control and relevant

research has been rarely reported. In this chapter, we focus our discussion on the monolayer template. A schematic drawing of a microbead monolayer is presented in Fig. 2.1a, b. Figure 2.1c shows the templated bottom structure after removal of the microbead monolayer. The inset in Fig. 2.1c is a cross-sectional view with a tilt angle of $\sim 30°$.

There are several types of driving force that induce microbeads to self-assemble into a dense monolayer [7]: capillary force when the solvent is evaporating; flux of the solvent, i.e., hydrodynamic steering during the evaporation process; increased Van der Waals force between neighbouring microbeads due to their high energy surface. The main contribution comes from the capillary force, as shown in Fig. 2.2 [6]. The capillary force or surface tension can be enhanced by adding surfactants into the colloid solution prior to the monolayer formation. For example, Triton-X-100, a typical surfactant, is generally used as an ingredient for dense packing of a microbead monolayer [8, 9]. The other contributors for the assembling driving force are discussed below.

The driving force is so strong that the monolayer can extend to centimetre (cm) size, as shown in Fig. 2.3. Due to the diffraction of light, a blue–purple colour is observed from the formed monolayer when the mean diameter of the microbeads is ~ 500 nm, which can be used as pre-screening to judge the success of a monolayer assembly [10].

Here, the monolayer deposition was conducted using spinning coating at 800 rpm on a silicon surface. The PS microbeads with a mean diameter of 500 nm were used directly without dilution ($\sim 10\%$ w/w in aqueous solution). Defects along the assembly domain boundaries (Fig. 2.3c) and within a domain (Fig. 2.3d) mainly originate from the non-uniformity of the microbead diameters, particularly considering the accumulation effect from sub-micrometre to centimetre during the monolayer formatting process. This hypothesis can be evidenced in Fig. 2.4, where the imaging position was kept unchanged while images were repeatedly collected every 5 min. We can see the movement of the microbeads in the marked areas, which is likely due to the static–electric interaction among the neighbouring microbeads resulting from the charging e-beam under the SEM operation. Therefore, the non-uniform diameters of microbeads are the main reason for

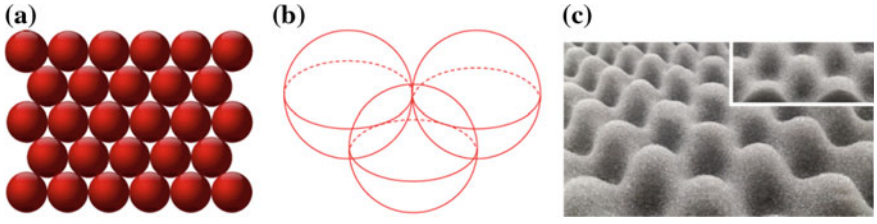

Fig. 2.1 **a** Schematic drawing of a microbead monolayer, **b** three neighbouring microbeads and **c** a photo-image of a templated bottom with a tilt angle of $\sim 30°$. The *inset* is a cross-sectional view

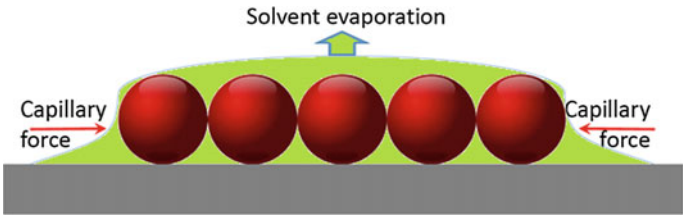

Fig. 2.2 Schematic drawing of the capillary force for a monolayer assembly

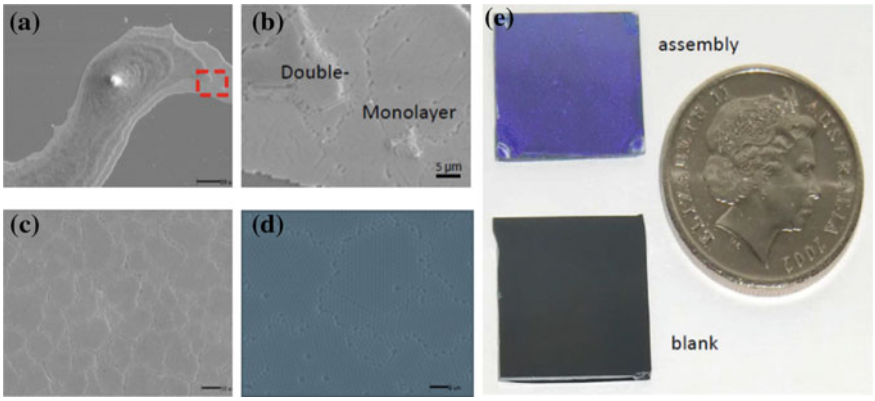

Fig. 2.3 **a**–**d** SEM images and **e** a photo-image of polymer microbead monolayers. **a** a Stacked multilayer, **b** a double layer and a monolayer, zoomed in from the marked area in **a**, **c** and **d** zoomed in monolayers, including boundaries and densely packed monolayer domains, and **e** an assembled monolayer with a bright *blue–purple* colour (*top*), which can be easily distinguished from the blank silicon wafer used for the assembly support (*bottom*). A *coin* is shown on the *right* to demonstrate the size of the monolayer assembly (Color figure online)

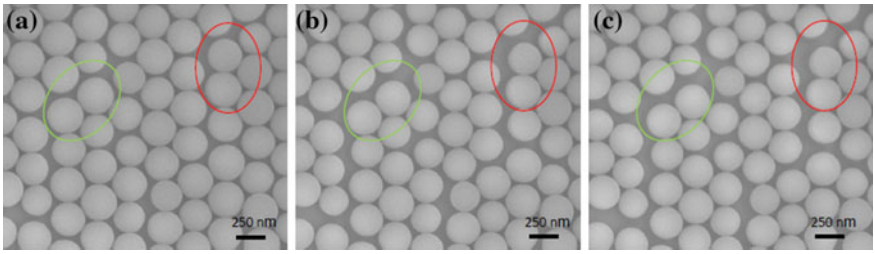

Fig. 2.4 SEM images at the same areas (*red* and *light green) ellipses* showing the movement of microbeads under the e-beam due to charging effects. The assembly conditions were the same as those in Fig. 2.3 except for the microbeads with a mean diameter of ~330 nm (Color figure online)

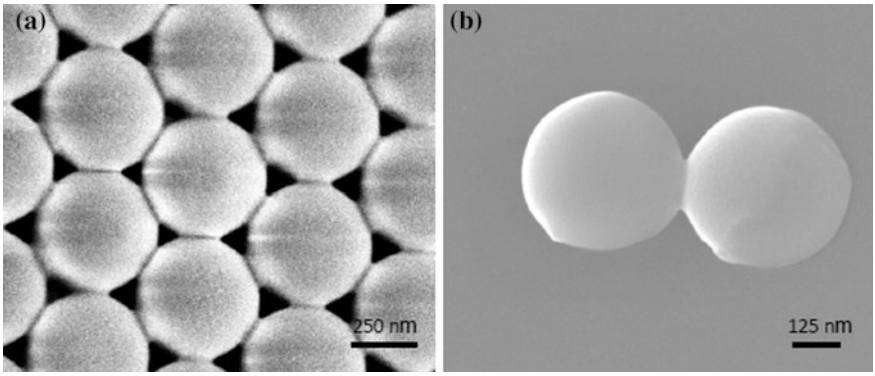

Fig. 2.5 SEM images of neighbouring microbeads. The deposition conditions were the same as those in Fig. 2.4

assembling defects and restriction into a dense monolayer scaling up to millimetre or even centimetre.

The high surface energy of polymer microbeads leads easily to the conjunction of neighbouring microbeads [11]. However, with respect of the conjunction, important contributing factors are the conditions of the assembly, such as solvent types, added surfactants, temperatures, ageing periods and aftermath treatment, as shown in Fig. 2.5. Fortunately, the junction has a limited effect on the subsequent templating process to fabricate nanostructures [12].

2.3 Fabricated Nanostructures

2.3.1 Templated Deposition

A simple method of fabrication of a nanostructure is the employment of microbeads as a template for deposition. Because the monolayer does not completely cover the support surface, leaving some voids, as shown in Fig. 2.1a, b, the deposition can occur on top of the monolayer microbeads and on the bottom of the monolayer. In the latter case, the deposition occurs directly on the monolayer support's surface through the voids, as shown in Fig. 2.1c. Deposition methods include electrochemical deposition [13, 14] and sputtering coating [3], as shown in Fig. 2.6. In the former case (electrochemical deposition), the template of the microbead monolayer should be kept stable in the deposition solution for the subsequent electrochemical reaction, and thus an annealing process is employed to plasticine the monolayer. After the annealing process, the polymer beads are connected (conjunction) due to their high surface energy. The plastic temperature might be significantly different from the bulk melting temperature, as discussed in the following.

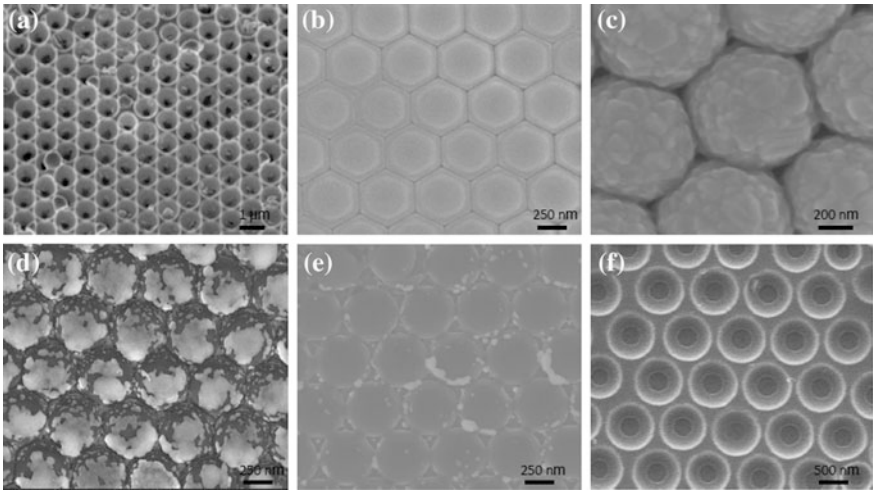

Fig. 2.6 SEM images of structures templated by polymer microbead monolayers. **a** Electrodeposited gold after lifting-off a microbead template (Reproduced from Ref. [14] with kind permission of © 2004 Wiley-VCH); **b** Microbead monolayer after sputter coating on the surface (as *ceiling*), and **c** Detailed morphology; **d**, **e** *Bottom* structure after lifting-off the monolayer template, **f** Templated PS by sinking of a monolayer assembly of silica. For the structures in **b**–**e**, the monolayer template was prepared according to Fig. 2.3. The deposited metals were ~30 nm titanium and ~300 nm silver. The subsequent washing off was carried out in toluene solution to lift-off the PS microbeads; **f** Porous PS preparation protocols are listed in main text

The advantage of electrochemical deposition is that the set-up is simple, and only an electrochemical workstation is required. However, selection of the deposition target is limited, as only materials that can easily be oxidised, electropolymerised, or reduced by the electrochemical system, can be deposited. The substrate/support for the monolayer template also needs to be conductive for electrochemistry, such as indium tin oxide (ITO). A representative structure is shown in Fig. 2.6a. In that case, deposition cannot occur on the top of the monolayer because the microbeads are not conductive.

In contrast, the sputtering coating process is more flexible. Some materials, such as carbon or aluminium that cannot be used in the electrochemical system, can be deposited using this approach. Furthermore, the monolayer's substrate/support can be glass/silicon because the conductivity of the substrate is not compulsory for the sputtering coating. Typical structures are shown in Fig. 2.6b, c before lift-off. After lifting off the microbead monolayer template, the bottom structures are shown in Fig. 2.6d, e. The difference between them lies in the extent of the lift-off. In Fig. 2.6d, the deposited shields/ceilings partly remain on top of the microbeads. In Fig. 2.6e, only the bottom is retained, while the top ceiling on the monolayer assembly has been completely removed.

A similar approach can be extended to the fabrication of polymer structures, such as the porous PS shown in Fig. 2.6f. The protocol is listed as follows:

(i) PS was dissolved into 1:4 toluene and spin coated on a silicon wafer surface to obtain a thin film of ~400 nm thickness; (ii) a silica monolayer template of microbeads with 500 nm diameter was deposited using the approach detailed above; (iii) incubation was carried out in toluene vapour for ~10 min to sink the silica monolayer into the polystyrene layer; and (iv) silica microbeads were removed by washing with hydrogen fluoride (HF, ~20%, w/w, ~5 min).

This is a bottom-up approach, i.e., the bulk structure was sunk/coined by a microbead monolayer template, not a top-down approach in which the deposition was templated by a microbead monolayer. With this method, we expanded the materials for nano-fabrication from electrochemically active materials such as gold, and sputter coating materials such as silver, gold, aluminium, carbon and titanium, to polymers in general.

Sometimes, microbeads need to be shrunk in an attempt to fine-tune the deposited nanostructure, as shown in Fig. 2.7. The shrinking might be conducted using argon or oxygen plasma. From Fig. 2.7a–c, the diameter of the beads has been gradually shrunk. Their templated and deposited nanostructures are shown in Fig. 2.7d–f. The deposited metal islands increase in size, when the diameter of the microbeads shrinks.

Not only have metal and polymer been deposited and templated by the microbead monolayers, but extra microbeads can also be templated. The extra microbeads are usually smaller than the primary beads, as shown in Fig. 2.8 [5, 6].

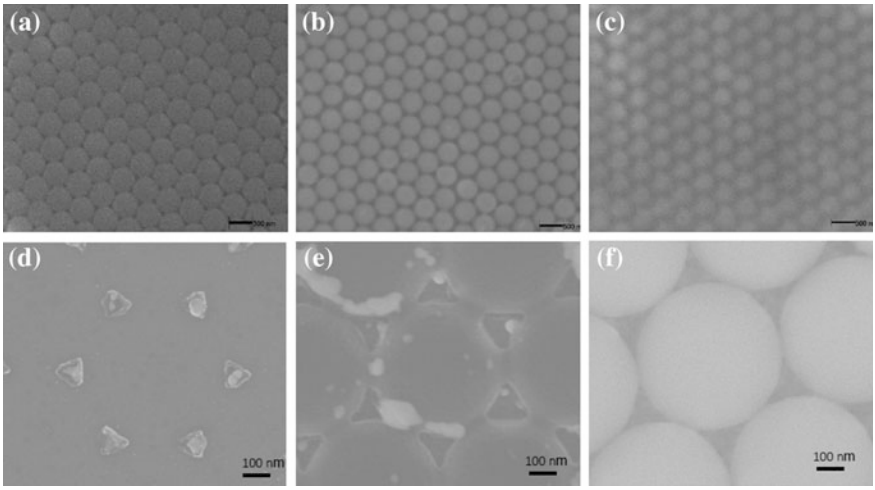

Fig. 2.7 SEM images of controllable nanostructures templated by microbead monolayers. The microbead monolayer was prepared according to Fig. 2.3. Oxygen plasma etching was carried out for different periods (**a**) 0 min, (**b**) 2 min and (**c**) 5 min. Their corresponding templated nanostructures are shown in **d**, **e** and **f**

Fig. 2.8 SEM images showing binary microbead monolayers (Reproduced from Ref. [5] with kind permission of © 2003 Wiley-VCH)

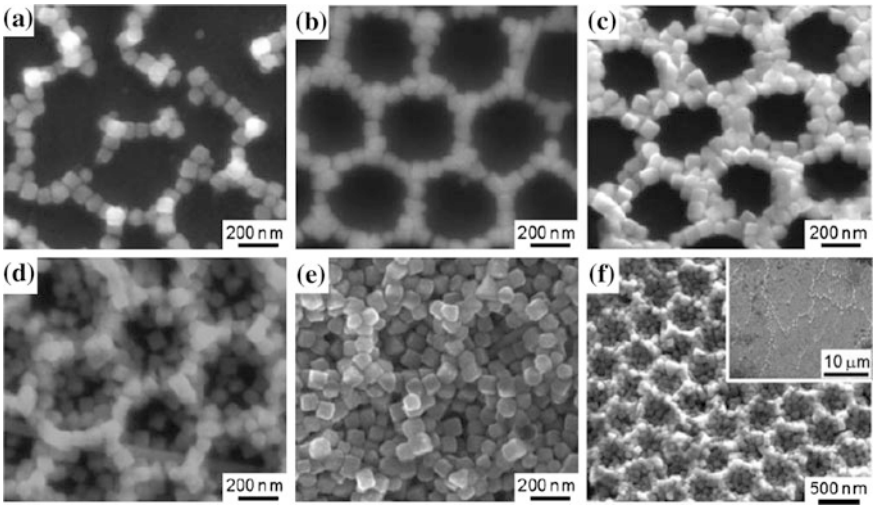

Fig. 2.9 SEM images of templated silver nanocubes. The polymer microbead monolayer was prepared according to Fig. 2.3. The deposition of nanocubes was carried out by dropping different concentrations of solution containing nanocubes and drying in air. Toluene was used to wash off the microbeads (Reused from Ref. [7] with kind permission of © 2013 Royal Society of Chemistry)

The driving force for the crystallisation structure was supposed to be the capillary force, as mentioned before.

Interestingly, the extra moieties can also be nanocubes, as shown in Fig. 2.9 [7]. We used this approach to build a high density of coupled nanocubes. The primary monolayer of microbeads works as islands to break the colloid liquid (containing nanocubes) into small areas as shown in Fig. 2.1a, b, with void areas less than μm^2. Within these small areas, the driving force for self-assembly from the capillary force of solvent evaporation is more efficient for arranging the nanocubes towards assembly. This assembly process within a small area (less than μm^2 rather than greater than cm^2) offers the possibility of densely packing the nano-moieties. That is, the monolayer template divides/grids the thin layer of solution containing

nanocubes into small areas, as shown in Fig. 2.2. Under the monolayer template, the void is small and the number of nanocubes is significantly reduced. Consequently, the assembly in this tiny void area is more operative than that in a large area without the monolayer template.

2.3.2 *Combination with Annealing*

To remove the polymer microbead monolayer template, in addition to the wash-off process with solvents, thermal annealing or de-wetting can also be used to remove the template by burning the polymer microbeads off. Annealing thus adds flexibility towards the nanostructure fabrication [4]. In terms of deposited silver, the annealing temperature is usually ~500–700 °C, which is lower than its bulk melting point (961.8 °C). The reason is due to the high surface energy of the nanostructure [15]. It has been reported that the surface atoms on the nanostructure, particularly at the tips or corners, look like liquid rather than solid [11]. This is because the nano surface means that the number of neighbouring atoms is much less than that in the bulk. The crystal grid is thus full of defects. Consequently, the surface atoms face less restriction than those in the bulk. The annealing approach and results are shown in Fig. 2.10. Basically, the silver ceiling on the top of the monolayer template or PS nanosphere mask shrinks into a nanoparticle, the size of which is dependent on the amount of deposited silver or the deposition thickness. Meanwhile, the silver

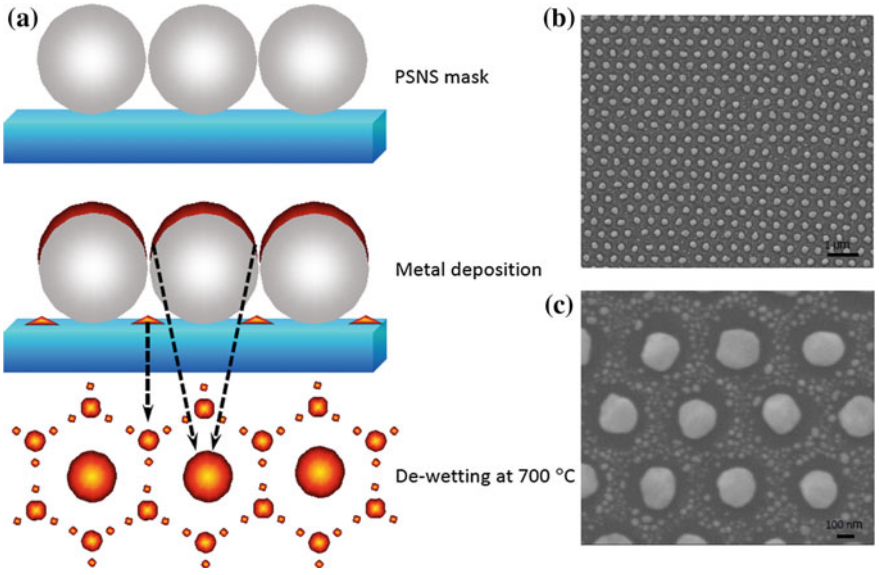

Fig. 2.10 **a** Schematic drawing and **b**. **c** SEM images of annealing results under different magnifications

deposited on the bottom void under the monolayer template shrinks into smaller nanoparticles to surround the central nanoparticles that stem from the ceiling shrinking.

For vertical deposition, different nanostructures can be fabricated by adjusting the annealing process, as shown in Fig. 2.11b, c. In removal of the template monolayer prior to the annealing process, the central nanoparticle is avoided and only the satellite nanoparticles remain. On the other hand, the tilting angle for the metal deposition also makes a significant difference [4], because it determines the deposition direction and the amount of metal for the subsequent annealing, as shown in Fig. 2.11. In Fig. 2.11d–e, with regard to the tilting deposition, it can be seen that the subsequent annealing leads to the appearance of the central nanoparticles without the surrounding satellite nanoparticles, which is contrary to the vertical deposition. In the meantime, by controlling the deposition amount, the size of the nanoparticles is also adjustable.

Annealing temperature and speed are other factors that should be considered, such as the melting point for bulk gold is 1064 °C vs. that of silver which is 961.8 °C. However, the annealing approach of gold is usually kept the same as the silver annealing profile since no obvious difference has been observed [4].

2.3.3 Combination with Etching

As known, metal can catalyse the etching reaction on silicon [4]. The underlying process is not fully understood but an electrochemical cell should be involved, which includes an anode for oxidisation of silicon and a cathode for reduction of oxidant or water, i.e., emission of hydrogen. Because polymer microbeads can feature a metal template of an ordered pattern on the silicon surface (discussed above), the subsequent catalysis etching fabricates an ordered nanostructure including female pores and male pillars, as shown in Fig. 2.12.

The sinking of a metal template into the silicon bulk can be evidenced from the etched structure in Fig. 2.12a. Basically, from the template fabricated from Fig. 2.7c, the deposited silver is treated by the toluene wash-off process to remove the polymer microbead monolayer. A porous silver film, akin to a net, remains on the silicon surface, as shown in Figs. 2.7f, 2.12a (inset). The silver net acts as a catalysis centre when silver-silicon is dipped into HF solution. Meanwhile, the void area without silver remains almost unchanged. The area covered with bulk silver film (not porous) is also maintained because it is shielded from the HF. Consequently, the array structure of the microbead monolayer is coined and sunk into the depth of silicon, as shown in Fig. 2.12a, b.

In Fig. 2.12a, along the boundary of the microbead monolayer domain, the etching morphology is different from that in the other parts. On the left of that boundary (dashed line), the etching is not obvious because the silicon/HF has been shielded by the silver film. On its right, when the silver template sinks into the silicon depth due to the etching, the silver net is stretched. Consequently, it does not

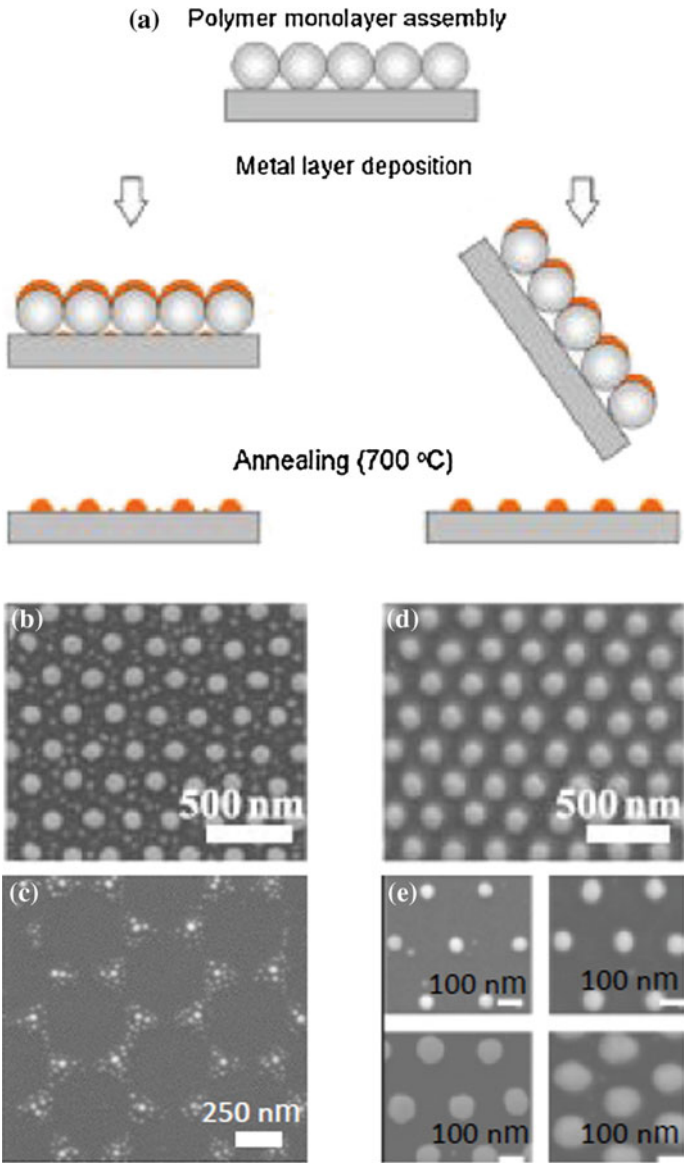

Fig. 2.11 Effect of deposition direction and amount. The microbead monolayer was prepared according to Fig. 2.3. **a** Schematic demonstration of a metal deposition and a subsequent annealing process; The vertically deposited ceiling layer of metal is kept (**b**) or removed (**c**) by using a solvent wash-off process prior to an annealing process; and **d**, **e** show the tilted deposition amount of the metal controlling the size of the annealed nanoparticles (Reproduced from Ref. [4] with kind permission of © 2013 Springer)

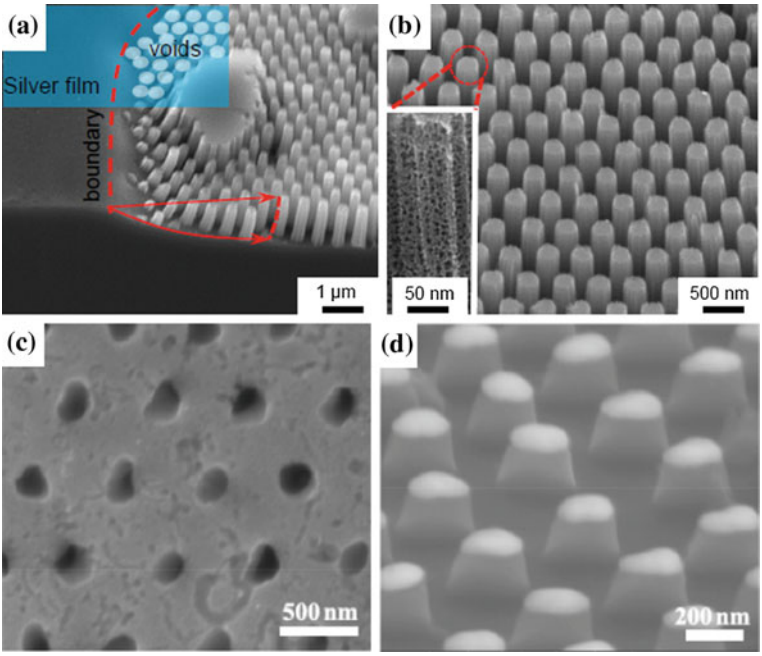

Fig. 2.12 SEM images of nanostructures of **a**–**c** wet etching and **d** dry etching. The polymer microbead monolayer was prepared according to Fig. 2.3. Then plasma etching occurred as illustrated in Fig. 2.7**c**, followed by metal deposition, toluene wash off and wet etching by dipping into a solution of 1:5:10 of HF–H_2O_2–H_2O (v/v) to obtain Fig. 2.12**a**, **b** structures. The *inset* in **a** schematically shows a metal template for the etching, and the *inset* in **b** shows the detailed structure. The metal nanoparticle array was prepared according to Fig. 2.11**d** and then followed by **c** wet etching or **d** dry etching (Reproduced from Ref. [4] with kind permission of © 2013 Springer)

sink directly and vertically into the bulk, rather than with an arc, as indicated by the arrow in Fig. 2.12a. Therefore, the pillar is not vertical to the etching surface but in the shape of an arc. Depending on the etching condition, the pillar left behind can also be porous, as shown in Fig. 2.12b (inset) [16–18].

In Fig. 2.12c, the female holes in the silicon were etched in a solution of HF–H_2O_2–H_2O with ratio of 1:5:10 (v/v) by the deposited metal's catalysis from the metal template as shown in Fig. 2.11d, a process which is called wet etching. Dry etching, on the other hand, features different structures, as shown in Fig. 2.12d. Dry etching is usually conducted using a plasma of reactive gases such as fluorocarbons [4]. It can effectively etch silicon, while the deposited metal can persist. Thus, metal (platinum) can shield and protect the silicon below to fabricate male pillars, as shown in Fig. 2.12d.

2.4 Applications

2.4.1 *Surface Plasmon of Templated Nanostructures*

Ordered structures have received increased attention recently due to their unique properties that cannot be expected in random structures. For example, an anisotropic nanostructure means that its surface plasmon will feature an anisotropic field, specifically an electric–magnetic field. When used as a SERS substrate, the enhancement will be anisotropic because the enhancement of the Raman signal stems mainly from the electric–magnetic field within the nanostructures, which usually are called as hot spots. If the arrangement of nanostructures such as nanocube assembly can be controlled, the distribution of hot spots on the SERS substrate surface can thus be controlled. In this case, the ordered structure means an ordered rather than random arrangement of hot spots. The resulting distribution of Raman intensity is uniform, as shown in Fig. 2.13 [7].

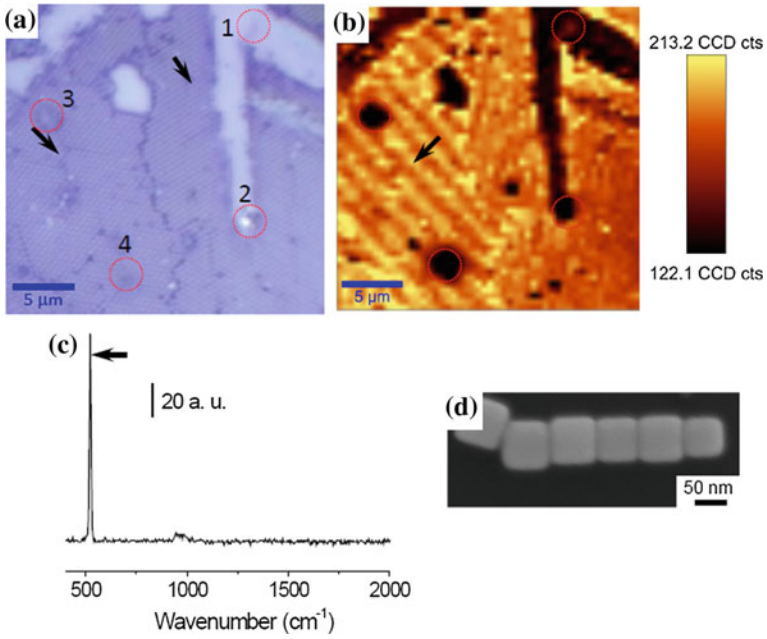

Fig. 2.13 **a** Silver nanocubes templated by a polymer microbead monolayer, **b** Raman mapping image based on **c** the silicon peak and **d** the coupled silver nanocubes. The preparation conditions of the nanocube pattern using polymer microbeads were given in Fig. 2.9**b** [4]. In Fig. 2.13**a**, **b**, the *marked areas* indicate (*1*) the non-ordered monolayer, (*2*) the stacked microbeads and (*3*, *4*) defects. The *arrow* directions in **a** and **b** are different due to the different signal collecting approaches, namely, (**a**) a photo-image and (**b**) a Raman mapping image (Reused from Ref. [7] with kind permission of © 2013 Royal Society of Chemistry)

Figure 2.13a shows a photo picture collected under microscopy. The domains of the microbead monolayer and their boundaries can be seen. These polymer microbeads were supported by the bottom silicon. The silicon's Raman peak at 519 cm^{-1} (shown in Fig. 2.13c) was collected to map its image, as presented in Fig. 2.13b. The similarity between the photo-image in Fig. 2.13a and the nanostructure distribution in Fig. 2.13b can be identified, confirming that the Raman enhancement originated from the nanostructure (hot spot), as shown in Fig. 2.13d. The uniformity of the enhanced Raman signal in the ordered nanostructure area can be seen in Fig. 2.13b, supporting the above hypothesis about the anisotropic field.

There are two important issues to be identified about hot spots, namely, the position of the hot spot and the electric–magnetic field intensity within the hot spot [2, 19, 20]. The former determines the robustness of the Raman signal (distribution and density), and the latter controls the intensity of the signal, the sensitivity and the limit of detection.

2.4.2 *Identification of Hot spot Position*

Simulation and calculation have suggested that there is a much higher electric–magnetic field around the corners of a nanocube than in the other areas [21–23]. Experimental proof was lacking, however, until a recent report [7]. One approach is demonstrated in Fig. 2.14 [7]. Basically, a self-assembled monolayer (SAM) of thio was used to cap a silver nanocube (AgNC) surface [24]. It has been reported that a SAM is always accompanied by defects/pinholes [25, 26]. In the primary SAM (A, 1-dodecanethiol, or DDT) formed on silver nanocubes ($\sim$50 nm), the defects/pinholes are most likely to be located on the corner. Therefore, the attacking position for the secondary thio (B, 2-mercaptopyridine, or MPy) occurs at the corner. Consequently, a mixture of SAM (A + B) is obtained with B on the corners, as shown in Fig. 2.14a–c with a pure SAM (B) shown in Fig. 2.14d for comparison. Using a microbead monolayer as a template, silver nanocubes were patterned as a SERS substrate with high enhancement (Fig. 2.14e). It can be found that Raman scattering intensity of molecule B is almost the same, regardless of from SAM (A + B) (MPy-DDT_AgNC) or from SAM (B) (MPY_AgNC), as shown in Fig. 2.14f, with peak heights marked by black lines. Therefore, the dominating position for SERS is on the corner, i.e., the hot spot position is on the corner.

Another approach is shown in Fig. 2.15 [27]. The gold nanocube surface, Fig. 2.15a, was capped and coated with a layer of silica, which was formed by dipping in a solution of tetraethylorthosilicate (TEOS). The corresponding structure is shown in Fig. 2.15b. Then the capped nanocube's coating was etched using NaOH. By carefully controlling the etching process, the corners were exposed while the other positions were still coated, as shown in Fig. 2.15c. A Raman probe of 1,4-benzenedithiol was then loaded onto the exposed gold corners due to the strong Au-S bonds, which could not be applied on the silica coating surface.

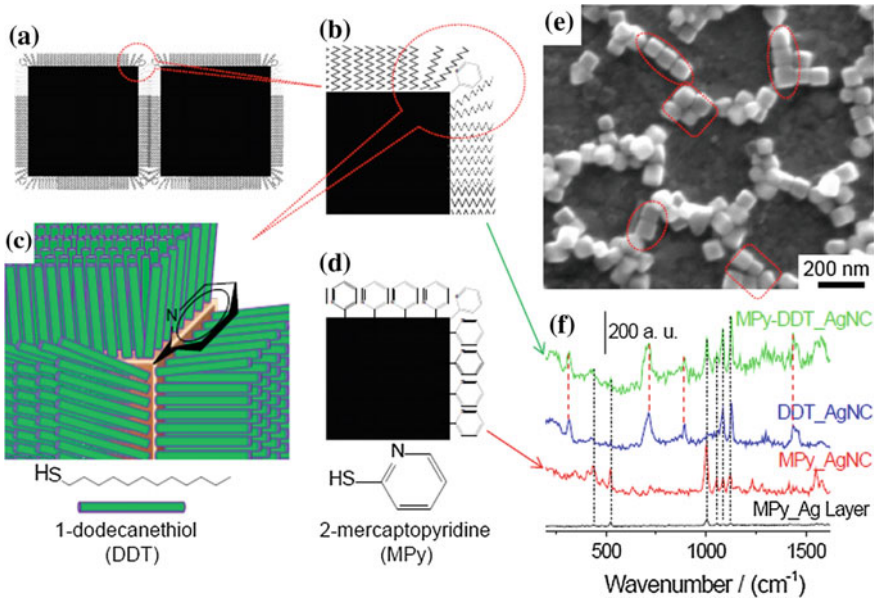

Fig. 2.14 **a**–**d** Schematic drawings of SAMs and **e** a SEM image of patterned silver nanocubes and **f** the Raman signals. The preparation conditions were described in Fig. 2.9**c**. Then the substrate was incubated in an ethanol solution containing 1-dodecanethiol (DDT) (0.1%, v/v) for 2 h (DDT_AgNC). After being washed off with ethanol and dried under a stream of nitrogen gas, the substrate was further incubated in an aqueous solution containing 2-mercaptopyridine (MPy) (10 μM) for 1 h (MPy-DDT_AgNC). Another substrate was prepared by directly incubating it in the MPy solution for 1 h (MPy_AgNC) [4]. For comparison, MPy standard Raman signals were collected from a silver film surface and presented (Reused from Ref. [7] with kind permission of © 2013 Royal Society of Chemistry)

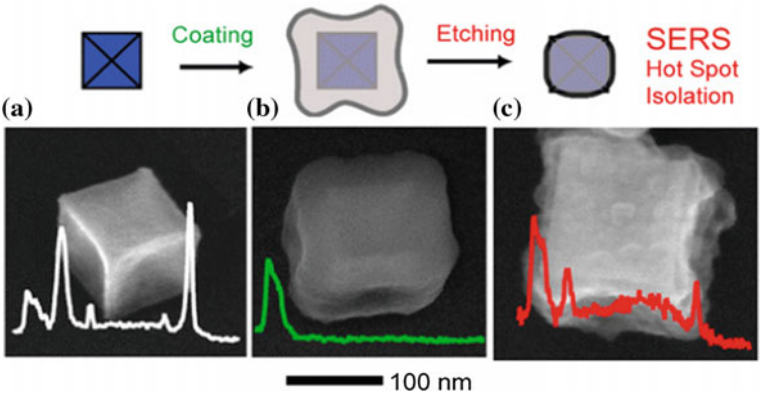

Fig. 2.15 Schematic drawing (*upper*) of the coating and etching approach and (*lower*) the corresponding results (Reproduced from Ref. [27] with kind permission of © 2012 American Chemical Society)

With the above process, the hot spots were chemically isolated and confirmed on the corner of the nanocube, as shown.

2.4.3 Single Molecule Detection

It is well known that SERS can reach single molecule detection [28, 29]. Here, another approach has been developed recently by us to demonstrate this single molecule detection [3, 7, 30, 31]. Two types of molecule have been selected here. In this bi-analysis approach, these two molecules (A and B) behave similarly in terms of loading affinity onto a SERS substrate, Raman activities, etc. Their concentrations are diluted (to the limit of detection) for single molecule loading, and their Raman signals have been mapped using their characteristic peaks and the results are shown in Fig. 2.16.

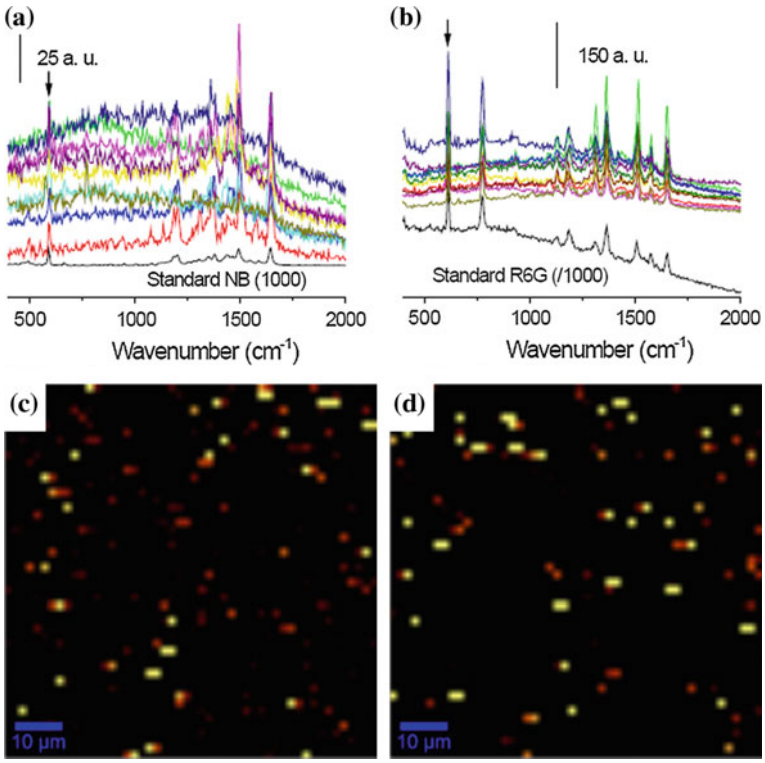

Fig. 2.16 Typical Raman spectra of **a** Nile blue (NB), **b** Rhodamine 6G (R6G) and **c**, **d** their corresponding mapping images. The Raman spectra in **a** and **b** were randomly collected at the *bright spots* in **c** and **d**, respectively. Their characteristic peaks are marked for the mapping (Reused from Ref. [7] with kind permission of © 2013 Royal Society of Chemistry)

Statistically, if a hot spot can be occupied by only one molecule, there are two possibilities, that it is occupied by A or by B, individually, not simultaneously, with similar possibility (~50% vs. ~50%). During the mapping process, the high-intensity Raman signals, corresponding to the bright dots in the mapping images, should originate from hot spots occupied by A or B individually, not simultaneously. Consequently, the bright spots in mapping image of A do not overlap on the bright spots in mapping image of B. Furthermore, the density of the bright spots in mapping images of A and B should be similar (~50% vs. ~50%). However, if a hot spot can contain two molecules, there are four possibilities, i.e. AA (~25%), AB (~25%), BA (~25%) or BB (~25%). In this case, there will be a ~25% chance of collecting pure A Raman signals from AA, another ~25% possibility of collecting pure B signals from BB, individually, not simultaneously. Meanwhile, we have a ~50% chance of collecting mixed signals from AB/BA, which maps as A, and also as B, simultaneously. Therefore, for the mapping images of A and B, we see that ~50% of bright spots will overlap. The map will feature an even higher overlapping percentage if a hot spot can contain three (~75%) or four molecules (~87.5%). Considering the variation of statistics, we believe that single molecule detection has been achieved when the overlapping percentage is less than 5%.

As mentioned, to reach the single molecule detection level or for a hot spot to catch only one molecule, the concentration must be low. That is, the solution needs to be diluted gradually for the individual Raman probe to be loaded on the SERS substrate surface, until we have <5% overlap from the collectable signals' mapping images. This concentration for a single molecule loading and detection is significantly dependent on the loading affinity of the Raman probe or the target molecule [3]. In other words, there are three main factors that should be considered for high-sensitivity SERS analysis: enhancement factor from the substrate, Raman activity and loading affinity. For example, we adjusted the concentration of Nile blue (NB) (10 nM) and Rhodamine 6G (R6G) (2 nM) in a bi-analysis solution (not the same), to reach the single molecule detection and balance their Raman signals [32], which has been echoed recently [33].

During the mapping process, the laser spot is around μm in size or smaller, depending on the focusing lens and the laser wavelength. The size of a hot spot, however, is in the nm range. Therefore, one laser spot could cover several hot spots, depending on the hot spot density on the SERS substrate surface. That is, a bright spot in the mapping image can be linked with one or more hot spots, as shown in Fig. 2.17. This complicates the statistical estimation of single molecule detection. On the other hand, the electric–magnetic field is high in the hot spot and the laser used for Raman excitation is intensive. As a consequence, during the signal collection process, there is a possibility that the molecule within a hot spot does not contribute to the Raman signal due to the shielding effect from laser excitation or from Raman scattering as marked with a red cross in Fig. 2.17, or from the photo-degradation (bleaching) of a Raman probe.

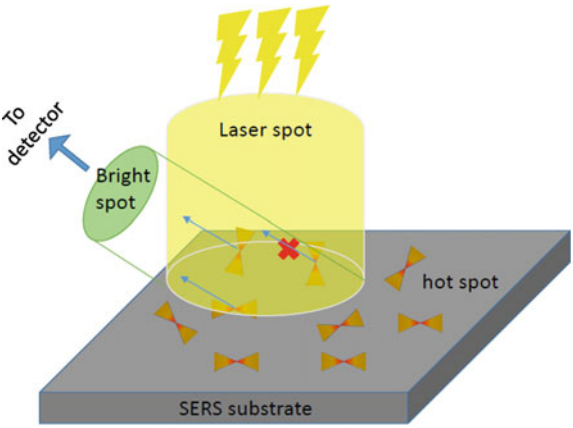

Fig. 2.17 Schematic drawing of Raman signal collection process

2.5 Summary

Polymer microbeads can be easily assembled into a monolayer for lithography to fabricate nanostructures via deposition, etching, annealing, etc. The templating targets include metals, semiconductors, polymers, nanobeads and nanocubes. Added together, there are many possibilities and much flexibility to fabricate various nanostructures. Fabricated nanostructures have various applications, such as SERS substrates to enhance Raman signals.

Acknowledgements We appreciate the funding and facilities support received from Flinders University (Adelaide, Australia), Leibniz Institute for New Materials (INM) (Saarbruecken, Germany), The University of South Australia (Adelaide, Australia), University of Newcastle (Newcastle, Australia), Cooperative Research Centre for Contamination Assessment and Remediation of the Environment (CRC CARE) (Newcastle, Australia) and the Australian Government, Department of Defence.

References

1. Haynes CL, Van Duyne RP (2001) Nanosphere lithography: a versatile nanofabrication tool for studies of size-dependent nanoparticle optics. J Phys Chem B 105(24):5599–5611
2. Jones MR, Osberg KD, Macfarlane RJ et al (2011) Templated techniques for the synthesis and assembly of plasmonic nanostructures. Chem Rev 111(6):3736–3827
3. Fang C, Bandaru NM, Ellis AV et al (2013) Beta-cyclodextrin decorated nanostructured SERS substrates facilitate selective detection of endocrine disruptor chemicals. Biosens Bioelectron 42:632–639
4. Brodoceanu D, Fang C, Voelcker N et al (2013) Fabrication of metal nanoparticle arrays by controlled decomposition of polymer particles. Nanotechnology 24(8):085304
5. Kitaev V, Ozin GA (2003) Self-assembled surface patterns of binary colloidal crystals. Adv Mater 15(1):75–78

6. Velikov KP, Christova CG, Dullens RPA et al (2002) Layer-by-layer growth of binary colloidal crystals. Science 296(5565):106–109
7. Fang C, Brodoceanu D, Kraus T et al (2013) Templated silver nanocube arrays for single-molecule SERS detection. RSC Adv 3(13):4288–4293
8. Cheung CL, Nikolić RJ, Reinhardt CE et al (2006) Fabrication of nanopillars by nanosphere lithography. Nanotechnology 17(5):1339
9. Lipson AL, Comstock DJ, Hersam MC (2009) Nanoporous templates and membranes formed by nanosphere lithography and aluminum anodization. Small 5(24):2807–2811
10. Fudouzi H, Xia Y (2003) Photonic papers and inks: color writing with colorless materials. Adv Mater 15(11):892–896
11. Roduner E (2006) Size matters: why nanomaterials are different. Chem Soc Rev 35(7): 583–592
12. Mitsui T, Onodera T, Wakayama Y et al (2011) Influence of micro-joints formed between spheres in coupled-resonator optical waveguide. Opt Express 19(22):22258–22267
13. Sun F, Cai W, Li Y et al (2004) Morphology-controlled growth of large-area two-dimensional ordered pore arrays. Adv Funct Mater 14(3):283–288
14. Sun F, Cai WP, Li Y et al (2004) Morphology control and transferability of ordered through-pore arrays based on the electrodeposition of a colloidal monolayer. Adv Mater 16(13):1116–1121
15. Moon K-S, Dong H, Maric R et al (2005) Thermal behavior of silver nanoparticles for low-temperature interconnect applications. J Electron Mater 34(2):168–175
16. Li X (2012) Metal assisted chemical etching for high aspect ratio nanostructures: a review of characteristics and applications in photovoltaics. Curr Opin Solid State Mater Sci 16(2):71–81
17. S-w Chang, Chuang VP, Boles ST et al (2010) Metal-catalyzed etching of vertically aligned polysilicon and amorphous silicon nanowire arrays by etching direction confinement. Adv Funct Mater 20(24):4364–4370
18. Chiappini C, Liu X, Fakhoury JR et al (2010) Biodegradable porous silicon barcode nanowires with defined geometry. Adv Funct Mater 20(14):2231–2239
19. Halvorson RA, Vikesland PJ (2010) Surface-enhanced raman spectroscopy (SERS) for environmental analyses. Environ Sci Technol 44(20):7749–7755
20. Haynes CL, McFarland AD, Duyne RPV (2005) Surface-enhanced raman spectroscopy. Anal Chem 77(17):338A–346A
21. Lee SY, Hung L, Lang GS et al (2010) Dispersion in the SERS enhancement with silver nanocube dimers. ACS Nano 4(10):5763–5772
22. McLellan JM, Li Z-Y, Siekkinen AR et al (2007) The SERS activity of a supported Ag nanocube strongly depends on its orientation relative to laser polarization. Nano Lett 7(4): 1013–1017
23. Wu H-L, Tsai H-R, Hung Y-T et al (2011) A comparative study of gold nanocubes, octahedra, and rhombic dodecahedra as highly sensitive SERS substrates. Inorg Chem 50 (17):8106–8111
24. Ulman A (1996) Formation and structure of self-assembled monolayers. Chem Rev 96(4): 1533–1554
25. Hakkinen H (2012) The gold-sulfur interface at the nanoscale. Nat Chem 4(6):443–455
26. Palmer RE, Robinson APG, Guo Q (2013) How nanoscience translates into technology: the case of self-assembled monolayers, electron-beam writing, and carbon nanomembranes. ACS Nano 7(8):6416–6421
27. Rycenga M, Langille MR, Personick ML et al (2012) Chemically isolating hot spots on concave nanocubes. Nano Lett 12(12):6218–6222
28. Bohn JE, Le Ru EC, Etchegoin PG (2009) A statistical criterion for evaluating the single-molecule character of sers signals. J Phys Chem C 114(16):7330–7335
29. Le Ru EC, Meyer M, Etchegoin PG (2006) Proof of single-molecule sensitivity in surface enhanced raman scattering (SERS) by means of a two-analyte technique. J Phys Chem B 110(4):1944–1948

30. Fang C, Xie Y, Johnston MR et al (2015) SERS and NMR studies of typical aggregation-induced emission molecules. J Phys Chem A 119(29):8049–8054
31. Fang C, Ellis AV, Voelcker NH (2012) Electrochemical synthesis of silver oxide nanowires, microplatelets and application as SERS substrate precursors. Electrochim Acta 59:346–353
32. Fang C, Shapter JG, Voelcker NH et al (2014) Electrochemically prepared nanoporous gold as a SERS substrate with high enhancement. RSC Adv 4(37):19502–19506
33. Zrimsek AB, Wong NL, Van Duyne RP (2016) Single molecule surface-enhanced raman spectroscopy: a critical analysis of the bianalyte versus isotopologue proof. J Phys Chem C 120(9):5133–5142

http://www.springer.com/978-3-319-57002-0

Polymer-Engineered Nanostructures for Advanced Energy Applications

Lin, Z.; Yang, Y.; Zhang, A. (Eds.)

2017, XXVI, 701 p. 382 illus., Hardcover
ISBN: 978-3-319-57002-0